DESIGN AND OPERATION OF A MICROGRID-BASED HYBRID ENERGY SYSTEM WITH A ZETA CONVERTER TO IMPROVE POWER QUALITY.

Naresh Kumar
University Poly.Electrical Engineering Section, Faculty of Engineering & Technology, Jamia Millia Islamia New Delhi, India.nkumar2@jmi.ac.in

Abstract
This paper addresses an approach that combines solar and wind energy to control a micro-grid in a distant place. The system features a double-fed induction generator and capacitor bank for converting wind energy. It has a solar PV panel and a DC-DC Zeta converter for converting solar energy. An indirect vector control with drooping properties is used to modify the voltage and frequency of the line-side converter. Due to the system's ability to modify the frequency dependent on the battery's energy level, it can run even when there is no wind. The maximum power point is also tracked using a fuzzy-based MPPT approach. The model is tested in a range of conditions, including as low battery charge levels, varying load types, and the absence of hybrid energy.The system operates automatically and addresses real-time issues, and an external power supply is available to charge the battery without requiring additional conditions.
Keywords*—PV, Double fed Induction Generator (DFIG), MPPT algorithm, Zeta Converter, PI controller, Fuzzy logic control (FLC) algorithm.*

I. INTRODUCTION

In many regions of the world, access to electricity might be restricted or sporadic, creating economic difficulties. One approach to solving this problem is to power an autonomous producing system using renewable energy sources like biomass, wind, and solar energy. While biomass energy sources are less practical due to supply chain issues, wind and solar energy sources are more environmentally friendly. They unfortunately cause power fluctuations and low utilisation rates due to their erratic behavior. Battery energy storage systems can be utilised to keep energy sources working at their peak efficiency to stabilise power production. Systems for controlling wind and solar energy employ power electronics components with MPPT control. Multiple-source hybrid energy systems can increase dependability and need less battery storage. Small-scale wind energy employs permanent magnet synchronous generators, whereas commercial wind energy frequently uses doubly-fed induction generators. The micro-grid system that is suggested in this study combines a DFIG for hybrid energy conversion. The study describes the design process and control techniques for all converters and presents simulation results using MATLAB. The control system assures high-quality power production in various operating situations.

II. SYSTEM COMPONENTS DESCRIPTION

A micro-grid with a renewable energy generating system (REGS) that can handle sites with a maximum demand of 15 kW and a mean power demand of 5 kW is shown in Figure 1. The

REGS is made up of two blocks: one for solar energy and the other for wind energy. Each block has a rated ability of 15 kW and a capacity utilisation factor of 20%, which is sufficient to cover the location's daily energy needs. The battery panel is connected to both the RSC and LSC, and in the case of insufficient wind speed, a 3-pole breaker can disconnect the wind source. While the LSC regulates the grid's voltage and frequency, the W-MPPT algorithm makes sure that the wind system spins at the appropriate rate for the RSC. Figure 2 depicts the energy flow, and the following subsections describe how the major REGS components were designed.

A. Aero Turbine Modeling:

The double-fed induction generator (DFIG) generates rotational energy from the mechanical energy of the wind, which is obtained through the wind turbine. An equation can be utilized to determine the amount of mechanical power produced through this process.

$$P_m = 0.5\ c_p\ \pi r^2\ \rho V_w^3 \qquad (1)$$

Wind speed and the radius of the wind turbine are denoted by the quantities Vw and r, respectively. The mathematical formula for the wind turbine's coefficient of performance, abbreviated Cp, is [13].

$$c_p(\lambda, \beta) = 0.73\left(\frac{151}{\lambda_i} - 0.002^{*}\ \beta^{2.14}\ -13.2\right)\ e^{-(18.4/\lambda_i)} \qquad (2)$$

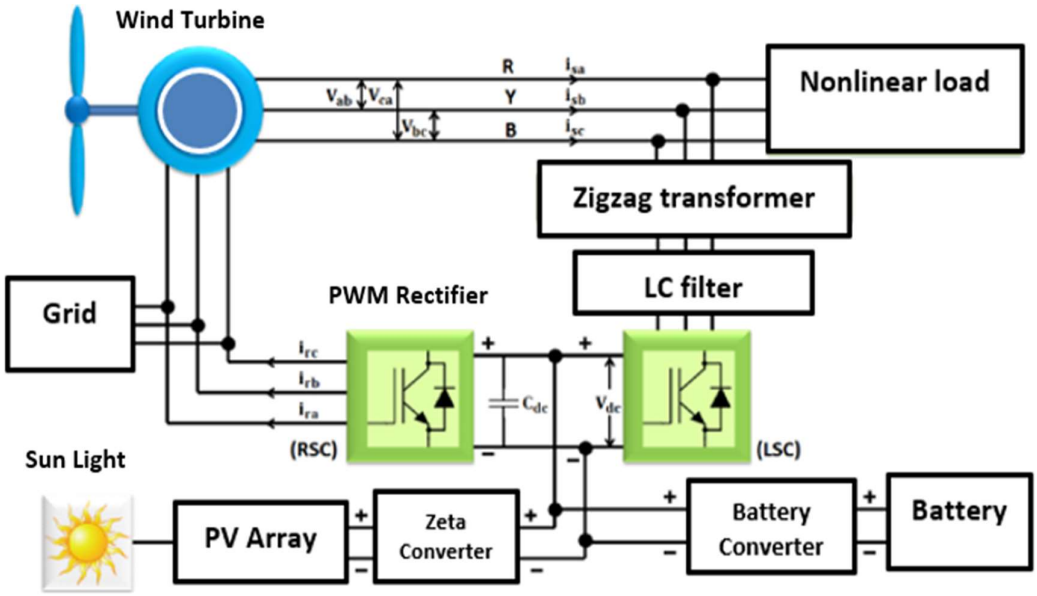

Fig 1.System block diagram

$$\frac{1}{\lambda_i} = \frac{1}{(\lambda + 0.08\ )} - \frac{0.035}{\beta 3 + 1} \qquad (3)$$

The terms λ and β denote, respectively, the tip speed ratio (TSR) and the turbine blade pitch angle. The following illustrates how TSR is related to the wind speed Vw, turbine speed r, and turbine radius r.:

$$\lambda = \omega_r r/(\eta_G V_w) \qquad (4)$$

$$\eta_G = \omega_{rm} r/(\lambda^{*} V_{wr}) \qquad (5)$$

where the turbine shaft gear ratio is denoted by η_G.The proposed system includes a wind generator with a 15 kW rated capacity, a 9 m/s rated wind speed, and a 198 rad/s rotating speed.

The Tip Speed Ratio (TSR) and turbine radius that work best are chosen to be 5.67 and 4.3 m, respectively. The gear ratio η_G is computed using equation (5) with the known values of *, Vwr, and rm to guarantee efficient operation. The control system is set to regulate the wind turbine at the Wind-Maximum Power Point Tracking (W-MPPT) until the machine speed hits rm.

$$\eta_G = (198x4.3)/ (5.67x9) = 16.68$$

B. Wind Generator:

When the wind speed is at its maximum and there are no losses, the nominal power output of the DFIG can be calculated using the rated air gap power (Pag) equation. Furthermore, the rotor and stator of the DFIG allow for external power transfer.

$$P_e=P_{ag}/(1+/S_{pmax}/) \quad (6)$$

The slip corresponding to the turbine speed rm is determined as Spmax, which is equal to -0.267, to calculate the speed range for the DFIG. The DFIG may operate at a range of speeds that correspond to slip values between 0.3 and -0.267. The electrical power rating of the DFIG (Pe) is computed to be 11.83 kW when the input power is at its maximum of 15 kW, assuming no losses, under the assumption that the rated air gap power (Pag) is equal to the mechanical input power.The 11.83 kW capacity of the DFIG is adequate to convert the 15 kW of mechanical power produced by the wind energy system into electrical energy since the RSC supplies the DFIG with the necessary magnetizing power while the wind turbine is in operation.

C. Zeta Converter:

Figure 1 depicts the proposed DC-DC Zeta converter, which is a better boost converter and SEPIC converter. L1 and L2 inductors serve as energy storage devices, with L2 ensuring high efficiency output current continuity. By acting as filters, capacitors C1 and C2 lessen voltage and current ripples. The converter's mode of operation, which can function as a Buck-boost converter with a
non-inverting output, is determined by the duty cycles.

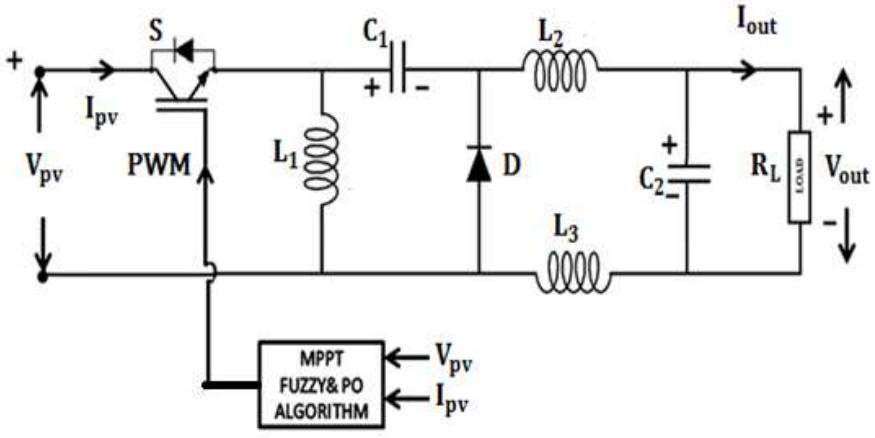

Fig 2. DC-DC zeta converter

The article presents a Zeta converter that can improve system performance by reducing double

frequency ripple in output voltages and achieving high output voltage gain at lower duty cycles. The converter's efficiency is further enhanced by using a fuzzy logic algorithm for MPPT. However, the presence of nonlinear loads can cause an increase in reactive power on the grid side, resulting in non-uniform current and reduced grid performance. The study discusses employing a PI controller for grid current compensation in order to address this problem. This technique helps to guarantee that the grid current and voltage are in phase, resulting in power factor operation that is close to unity. The suggested system may provide high voltage stability on the grid side as a result of these advancements.

D. Grid Side Transformer:

To establish a connection between the load and stator terminals with the Load-Side Converter (LSC) and provide a neutral point for single-phase loads operating at 415 V, a zig-zag transformer is employed in the system. This transformer serves the purpose of matching the maximum rotor voltage, Vrmax, which occurs at a rotor slip of 0.3. The transformer is designed with a voltage ratio of 415/125 V, where the low voltage (LV) side is set to 125 V (0.3 x 415 V) to achieve this matching.A 20 kVA transformer is selected to accommodate the combined kVA requirements of the load and connected filters, as well as to fulfill the reactive power demand during peak load conditions..

E. Battery Capacity:

The most operating slip of 0.3 is used to calculate the necessary DC bus voltage (Vdc) for pulse-width modulationcontrol. This slip corresponds to a DFIG speed of 110 rad/s and a rotor line voltage of 125 V (which is 0.3 times 415 V).

$$V_{dc} > \{2\sqrt{(2/3)}V_L\}m_i \quad (7)$$

The difference in voltage between the LV side of the zig-zag transformer and the rotor voltage at the maximum operating slip of 0.3 is used to compute the necessary DC bus voltage (Vdc) for pulse-width modulation control, which is 125 V. According to the assumption that the modulation index is unity, the minimal DC bus voltage needed for PWM control is 204 V. However, this system makes use of a 240 V DC bus voltage. The rotor voltage reaches its maximum value of 125 V at the DFIG's maximum slip of 0.3, which translates to a speed of 110 rad/s.

The proposed micro-grid aims to sustain a 5 kW load for 12 hours without any power generation source, accounting for 20% energy transfer losses. This requires a battery storage capacity of 72 kWh. Based on the 240 V DC bus voltage, the battery's AH rating is calculated as 300 AH (72,000/240). To achieve this rating, 40 lead-acid batteries with a 12V and 150 AH rating are connected in two parallel circuits.

With a maximum and lowest voltage of 270 V and 216 V, respectively, the safe voltage range for a lead-acid battery bank is in the range of 2.25 V and 1.8 V per cell. Modelling a battery bank as a DC source with a parallel resistor Rb to allow for self-discharge and a series combination of an imaginary capacitor C_b and internal resistance Rin is possible. The value of C_b can be calculated using a formula provided in a reference source [14].

$$C_b = \text{kWh} \times 3600 \times 1000/\{0.5 \times (V_{bmax}^2 - V_{bmin}^2)\} \quad (8)$$

After replacing the variables in equation (8), the value of C_b is calculated to be 19753 F.

F. Solar Requirements:

Rey-Boue et al. [15] discussed that PV cells are the building blocks of a solar PV system, and to prevent the OC voltage of the PV from exceeding either the DC bus voltage or the minimum downstream voltage of the solar converter, the solar panels are arranged in a specific configuration. The number of cells in a string (Nc) is calculated based on the DC voltage and the Vocc of each cell, using the following equation:

$$N_c = V_{dc} - Vocc/V_{occ} \quad (9)$$

To ensure that the Vocc of the PV remains within safe limits, the solar PV system employs a particular arrangement of solar cells, which are the primary component of the system. The number of cells in a string, Nc, is calculated using equation (9) with a maximum DC bus voltage, V_dcm, of 210 V, a maximum variation of 3% in the solar array voltage, us, and a minimum battery voltage of 216 V. Assuming a Vocc of 0.64 V, 328 cells are required, distributed among nine modules, with 36 cells per module. With a typical module with a Vocc to cell voltage at MPP ratio of 1.223, the module voltage at MPP (V_mpc x 36) is 18.83 V, whereas the solar array voltage (us) is 169.47 V. Table I lists the specific parameters for the solar energy block. 11 strings are chosen to obtain a cumulative string current at MPP of 88.5 A with a solar array capacity of 15 kW and a module current at MPP (Imp) of 8.04 A, which is equivalent to a short circuit current, Isc, of 8.69 A based on the Isc to Imp ratio of the usual module.

G. Filter Design:

To stop voltage fluctuations, a high pass filter is used at the DFIG's stator terminal. The temporal constant of this filter has to be smaller than the fundamental frequency of 20 ms. Additionally, the filter should be set to half the switching frequency, which is 10 kHz, necessitating the use of a 5 kHz filter. To do this, a series RC filter with a 15 F capacitance and a 5 R resistance is connected to the stator terminals. To harmonic voltages with frequencies higher than 5 kHz, this filter has an impedance of less than 5.43.

III. CONTROL ALGORITHM

The control descriptions for the three converters that make up REGS are provided below, as shown in Figure 1.

A. Control of Zeta Converter

A boost-type Zeta converter with an S-MPPT logic system is used to collect solar energy. This converter uses fuzzy logic to maintain the solar system's maximum power point (MPP) by intelligent switching. Figure 3 displays the flowchart for the MPPT algorithm.

B. LSC Control:

The design includes two power components to guarantee continuous system functioning in cases when wind power is unavailable for 60–70% of the time owing to onshore wind turbine restrictions. The DFIG's current power when the wind turbine is running is represented by the first component, iqs1. The DFIG's current power while the stator is not attached to the load terminal is represented by the second component, iqs2.Additionally, the generator's common

connecting point's reactive power consumption is considered and is expressed by ids*. The values of iqs* and ids* are used as reference stator currents to maintain voltage and frequency using an indirect vector control approach. The LSC is responsible for controlling the stator frequency, incorporating a droop characteristic to establish a frequency set point and ensure that the system generates power at the rated frequency.

$$\omega_e^*= 2\times \pi\times [50+ \{V_{dc}- 240)/ (V_{dcmax}-V_{dcmin})\}] \quad (10)$$

The system's frequency is determined by considering the lowest (Vdcmin), highest (Vdcmax), and current DC bus voltages. Vdcmax is set at 272.5 V, which represents the maximum bus voltage during battery charging (Vbmax). Conversely, Vdcmin is set at 213.5 V, indicating the minimum bus voltage during battery discharge (Vbmin). Using these values, the frequency range is calculated to be between 49 Hz and 51 Hz.

The calculation for ids* involves utilizing a formula to determine the magnetizing component of the stator current required at the load terminal. It is represented as follows:

$$i(ds(k))^* = i(ds(k-1)) + Kpv(v(err(k)) - v(err(k-1))) + Kiv\ v(err(k))\ dt \quad (11)$$

Where v_(err(k)) represents the voltage error, calculated as:

$$v(err(k)) = VLm^* - V(Lm(k)) \quad (12)$$

On a per-unit line level, VLm is the amplitude of the measured three-phase line voltage at the generator terminals. The following formula is used to calculate it from the detected line voltages (VLab, VLbc, and VLca):

$$VLm = \{2(vLab^2 + vLbc^2 + vLca^2)/3\}^(1/2) \quad (13)$$

The reference line voltage, VLm^*, is kept at 585 V.
Regarding the computation of iqs^*, it is divided into two sub-components:

$$iqs = iqs1 + iqs2 \quad (14)$$

The quadrature component of the generator along the stator field is represented by iqs1* and is calculated as:

$$i(qs1(k)) = -Lm * i(qr(k))/Ls \quad (15)$$

When the Doubly Fed Induction Generator (DFIG) is not linked to the Load-Side Converter (LSC) owing to low wind speed or faults, iqs2 is the necessary quadrature component of the stator current. It receives the following rating:

$$i(qs2(k))^* = i(qs2(k+1)) + Kp\omega e(\omega(eerr(k)) - \omega(eerr(k-1))) + Ki\omega e\ \omega(eerr(k))\ dt \quad (16)$$

The error between the rated frequency e and the actual frequency e is represented by w(eerr(k)), which was computed using Equation (10). The AC quantities (i(sa)), i(sb)), and i(sc)) are converted from the estimated DC quantities of i_(ds)* and i(qs)* using the angle statorflux, which is derived by integrating e over time.:

$$\Theta\text{statorflux} = \int 0\text{^}1\ \omega e\ dt \qquad \theta_{\text{statorflux}} = \int_0^1 \omega_e^* dt \qquad (17)$$

The transformation angle θstatorflux is used to convert the values of ids and iqs into 3-phase quantities. The hysteresis current regulator uses the resulting 3-phase quantities and detected stator currents to generate switching pulses. The RSC is responsible for controlling the turbine's speed to maintain MPP and provide magnetizing power to the generator. The controller algorithm, depicted in Figure 5, calculates Iqr and Idr, as well as the transformation angle θslip. The calculation of idr* is essential for the FOVC of the magnetizing power through the RSC, and idr is determined based on the no-load magnetizing power.

$$i_{dr}^* = I_{ms} = V_{Lm}^* / (\sqrt{3}X) \qquad (18)$$

i_{qr}^* is derived from output of the PI speed controller as,

$$i_{qr(k)}^* = i_{qr(k+1)} + K_{p\omega e}(\omega_{rerr(k)} - \omega_{err(k-1)}) + K_{i\omega e}\omega_{rerr(k)}\,dt \qquad (19)$$

K_{pr} and K_{ir} are proportional and integral gains of PI speed controller.$\omega_{rerr(k)}$ is speed error between reference and sensed speed as,

$$\omega_{rerr(k)} = \omega_{r(k)} - \omega_{r(k)}^* \qquad (20)$$

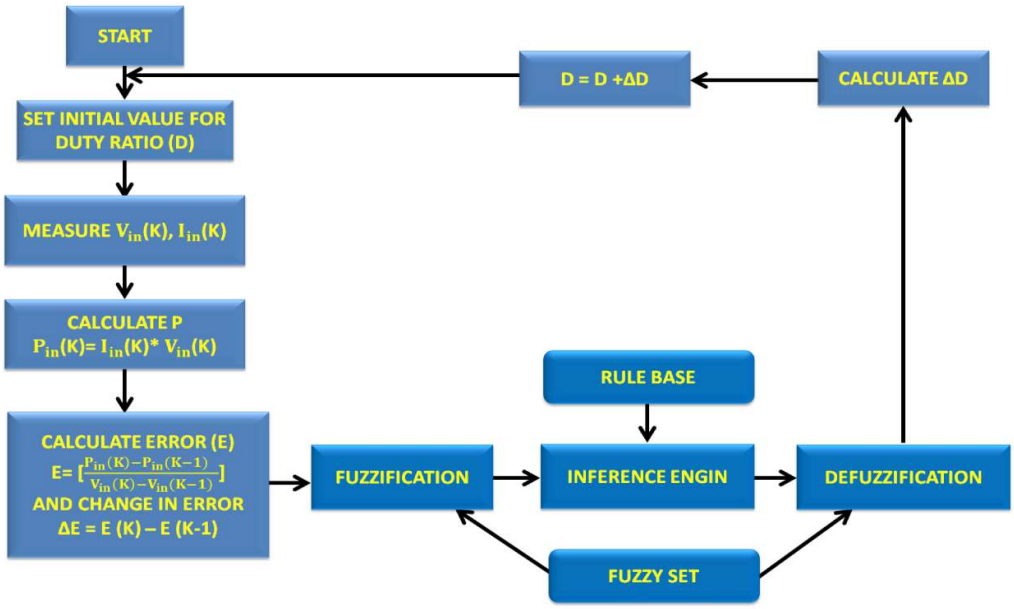

Fig 3. Flow-diagram of FLC MPPT algorithm.

$\omega_r^*$is reference speed which is derived from (5) as,

$$\omega_r^* = k \times \eta_G \times V_w / r \quad (21)$$

The wind speed reference is modified by a fixed value 'k' to avoid overvoltage when the production is high and the load demand is low. When DC bus voltage goes beyond 260 V, the relay output is reduced to 0.85, and when it exceeds 265 V, it is further reduced to 0.72. This adjustment in 'k' is done to prevent voltage rise in such situations.

The computation of the transformation angle θslip is based on a formula that uses the reference values of idr^* and iqr^, and its output is used to transform these values into AC rotor currents (ira, irb* and irc*).

$$\theta_{slip} = \int_0^1 (\omega_e^* - (p/2)\omega_r) dt \quad (22)$$

The control gestures for the RSC are produced by the hysteresis current regulator using error signals derived from the suggestion currents and perceived currents (i_ra, i_rb, and i_rc).

IV. RESULTS

The suggested method was validated by the MATLABSimulink package. Tables 1 and 2 present the specifications and ratings of the PV and Zeta converter, respectively.

Table 1. Specifications for PVmodule.

COMPONENTS	RATINGS/ SPECIFICATIONS
Number of panels	30
Number of cells in series	36
Cell	125mm×31.25mm
Open circuit voltage	21.4V
Optimum operating voltage	16.8V
Short circuit current	1.21A
Optimum operating current	1.19A
Operating temperature	-40 to +85^{0}C
Maximum system voltage	1000V DC

Table 2. Requirements of zeta converter

Components	Symbols	Rating
Source Voltage	v_{in}	0 to 300 V DC.
Source Current	i_i	75 A (Max)
Capacitors	C_1,C_2	20uF
Inductor	$L1, L2$	7mH
Output load current		60 Amps
Switching frequency	f	10 KHZ
Output Power	P_0	15kW

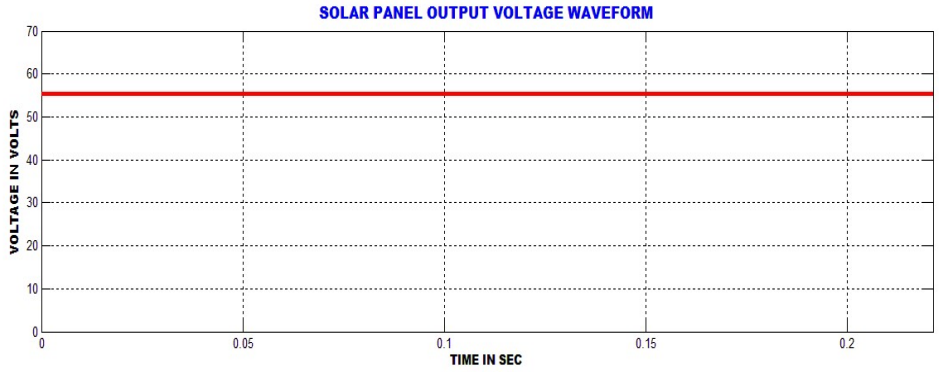

Fig 4. PV output voltage

The illustration displays a voltage waveform obtained from a solar panel that is constructed by connecting 36 solar cells in parallel and series. The measurement was taken at a constant temperature of 25 degrees Celsius and an irradiation level of 1000 W/m2. The generated output voltage is then fed into the Zeta converter to boost its voltage level.

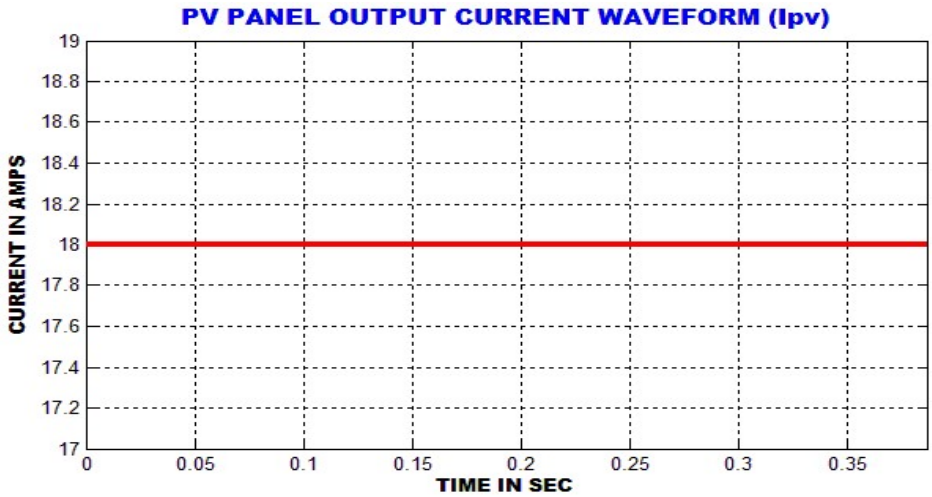

Fig 5. Solar panel output current waveform

The current waveform produced by the solar panel, also known as Ipv, is illustrated in the figure. This waveform is used in conjunction with the voltage generated by the solar panel, Vpv s, as the input parameters for the FLC MPPT algorithm.

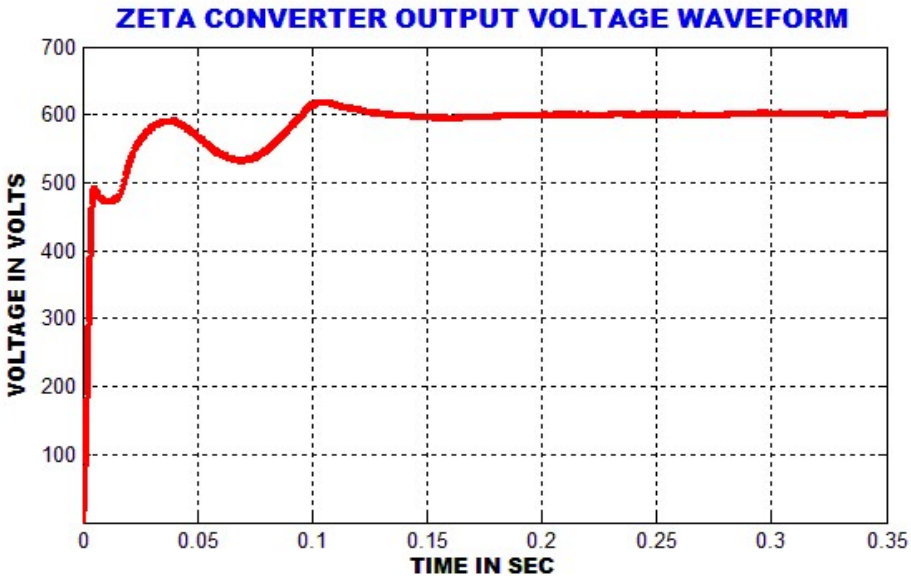

Fig 6. output voltageof Zeta Converter

The aim of the FLC algorithm is to achieve a constant output voltage while maximizing the power output of the PV. The Zeta-converter is employed to reduce fluctuations in the voltage waveform, resulting in a steady DC voltage suitable for powering AC loads through a three-phase inverter. Furthermore, this DC voltage can be utilized to store energy in batteries using the battery converter.

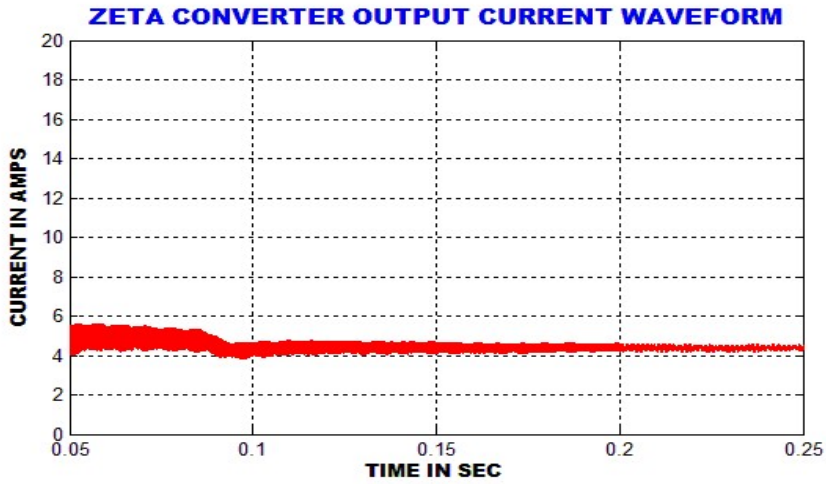

Fig 7. Zeta Converter output current waveform

The graph presented illustrates the Zeta converter's output current waveform, which indicates that the converter operates without any disruptions, resulting in a constant current output. The efficient functioning of the converter greatly influences the performance of the photovoltaic (PV) system.

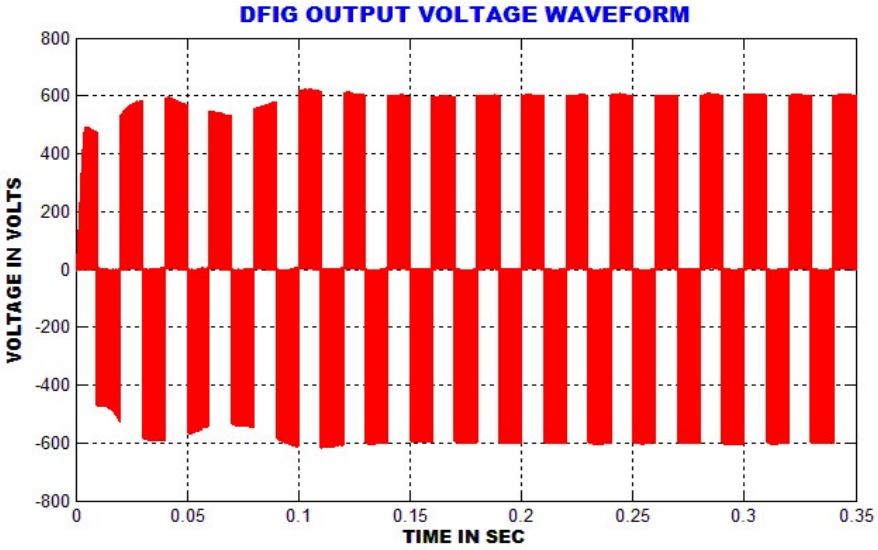

Fig 8. output voltage of DFIG

The voltage waveform of the DFIG that is affected by wind speed variations is displayed in the diagram. This voltage waveform is subsequently input into the PWM rectifier.

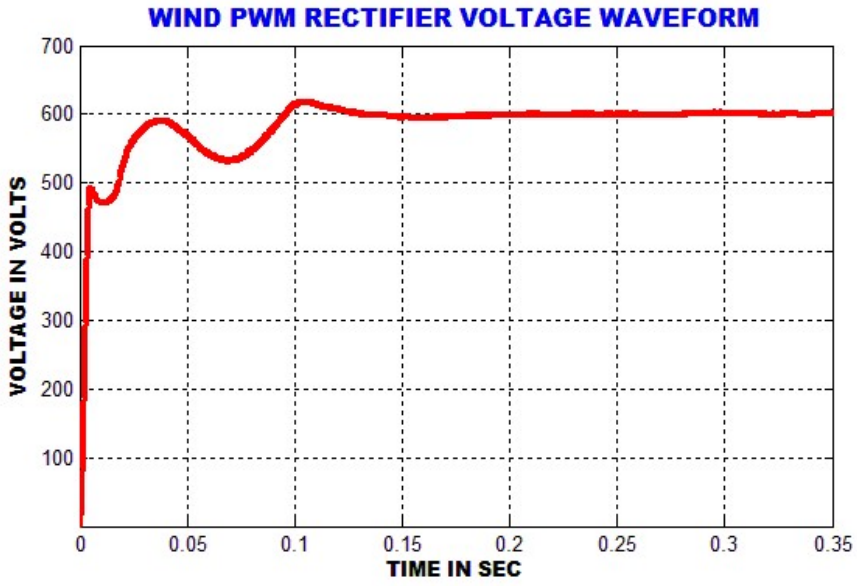

Fig 9. PWM Rectifier output voltage waveform

The graphical representation illustrates the output voltage waveform obtained from a Pulse Width Modulation (PWM) rectifier. This waveform is achieved through closed-loop control utilizing a PIcontroller. The primary goal of utilizing the PI controller is to ensure the stability and seamless nature of the output voltage waveform produced by the rectifier's PWM (Pulse Width Modulation.

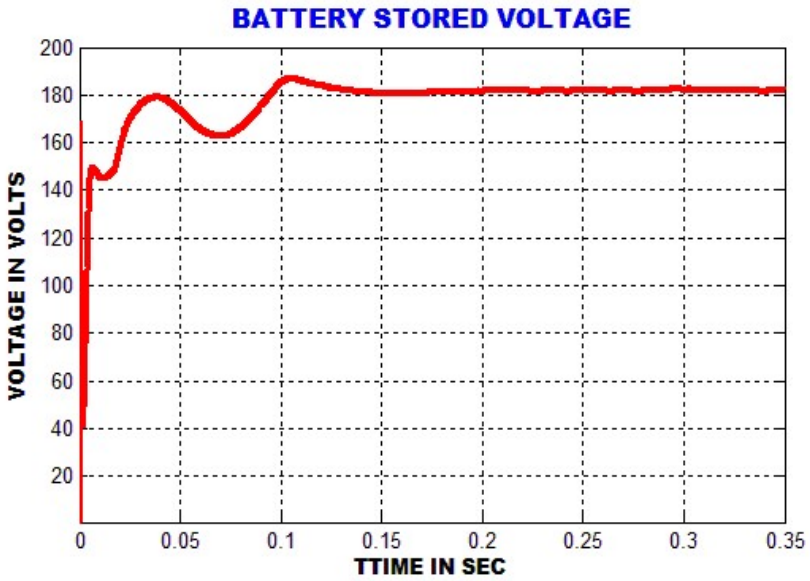

Fig 10. Voltage of Battery.

The figure illustrates the battery voltage, which is achieved using a bidirectional battery converter capable of both charging and discharging the battery. During the charging phase, the converter functions in buck mode, while during the discharging phase, it operates in boost mode.

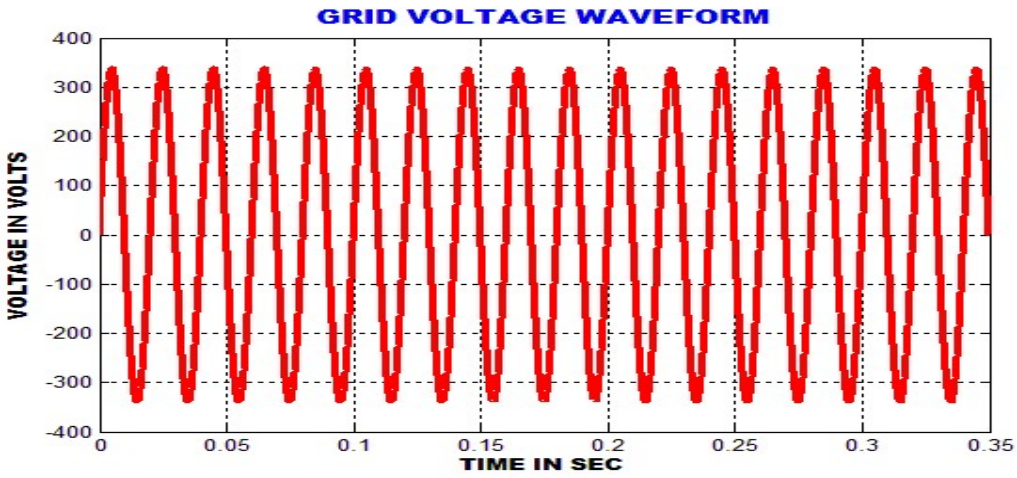

Fig 11. Grid voltage waveform

The figure illustrates the waveform of the grid voltage that is succeeded using a hysteresis current controller that is synchronized with the grid. To ensure that there are no harmonics in the output voltage and grid current waveforms, a PI controller is used for grid synchronization. By implementing grid synchronization techniques, the sinusoidal pattern of the grid V and I is achieved.

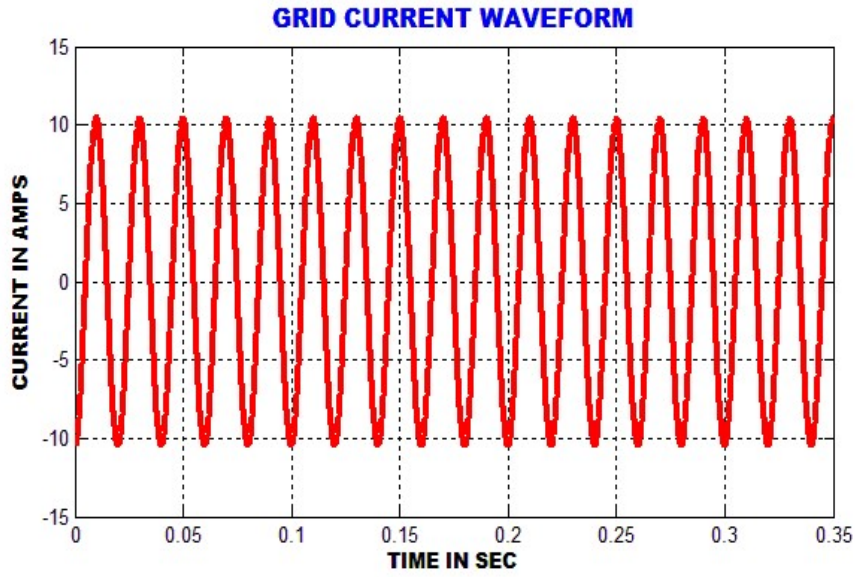

Fig 12. current at grid

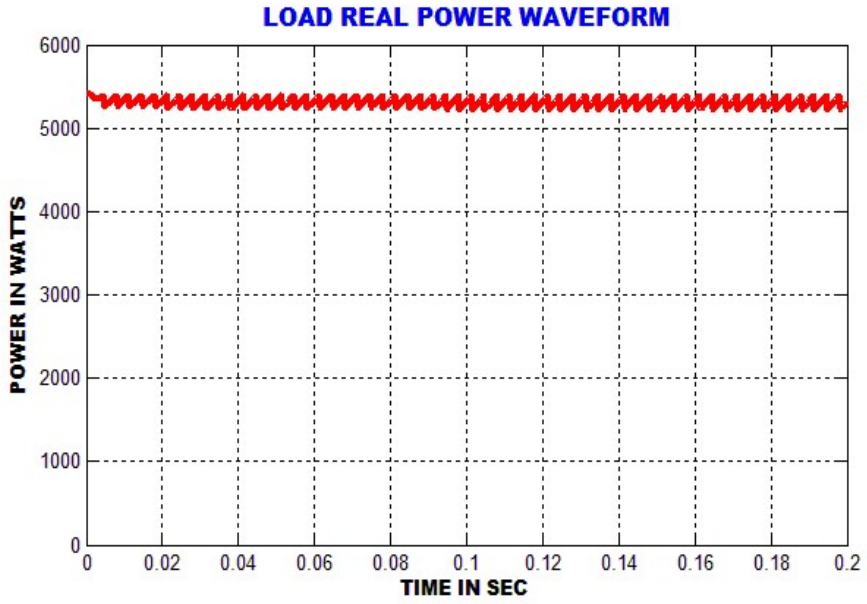

Fig 13. Load true power.

The given figure represents the active power on the load side, which is attained by utilizing PI-based compensation technique that helps in minimizing reactive power and enhancing the production of active power. This approach also ensures stable voltage operation during steady-state conditions.

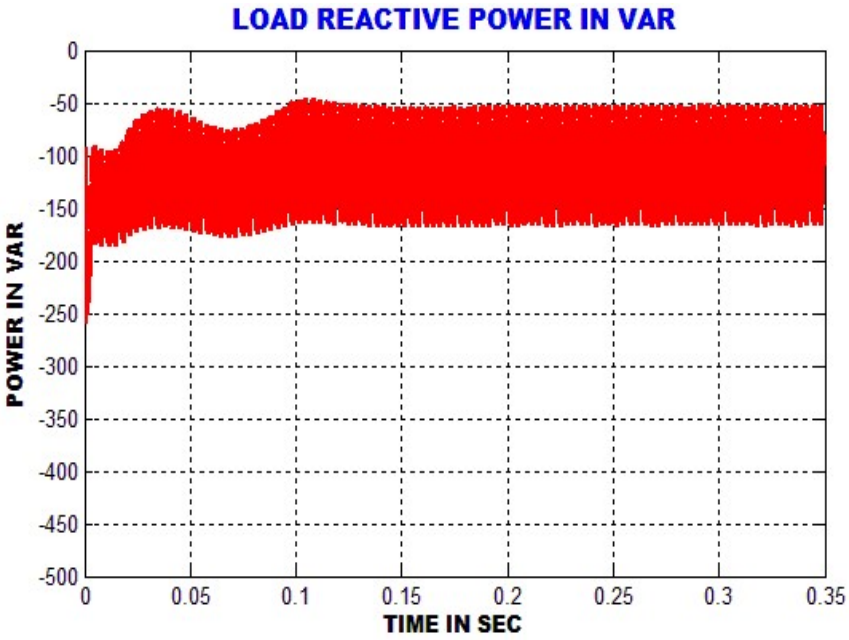

Fig 14. Load Reactive power

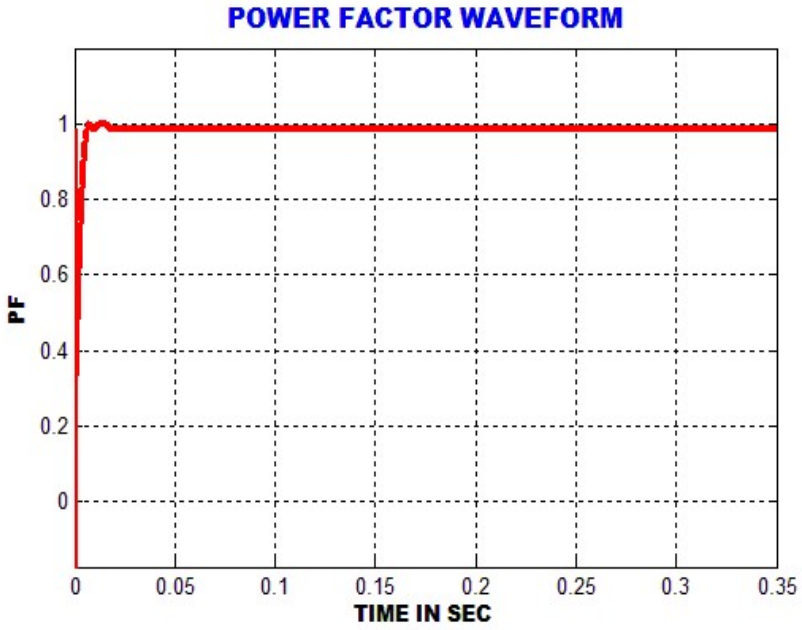

Fig 15. Load Power factor.

The diagram shows the power factor on the load side, which is attained through the use of a hysteresis current controller synchronized with the grid, aimed at keeping the power factor close to unity. In addition, a PI controller prioritizes real power over reactive power to optimize the generation of real power, resulting in a unity power factor operation, reducing power quality problems.

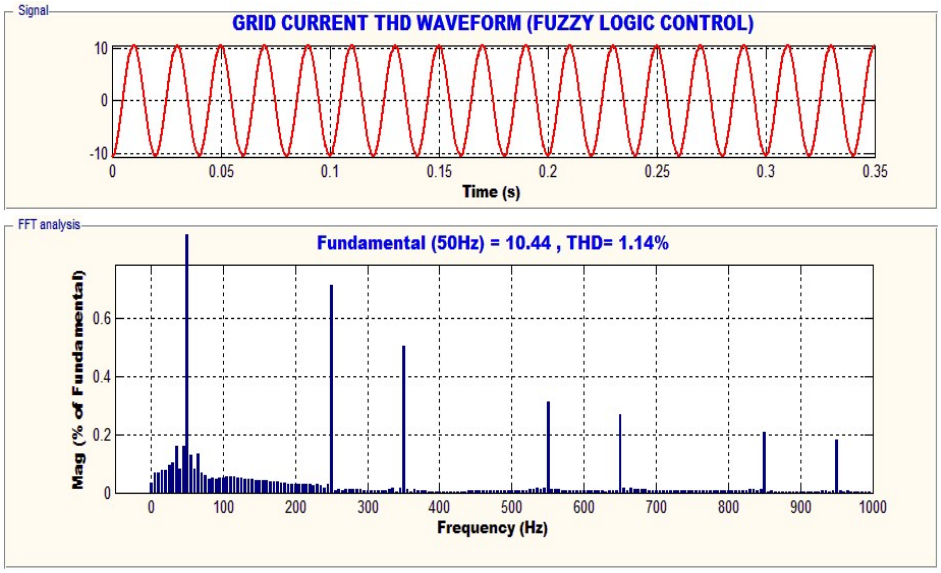

Fig 16. The FLC technique is utilized to generate the grid current THD waveform.

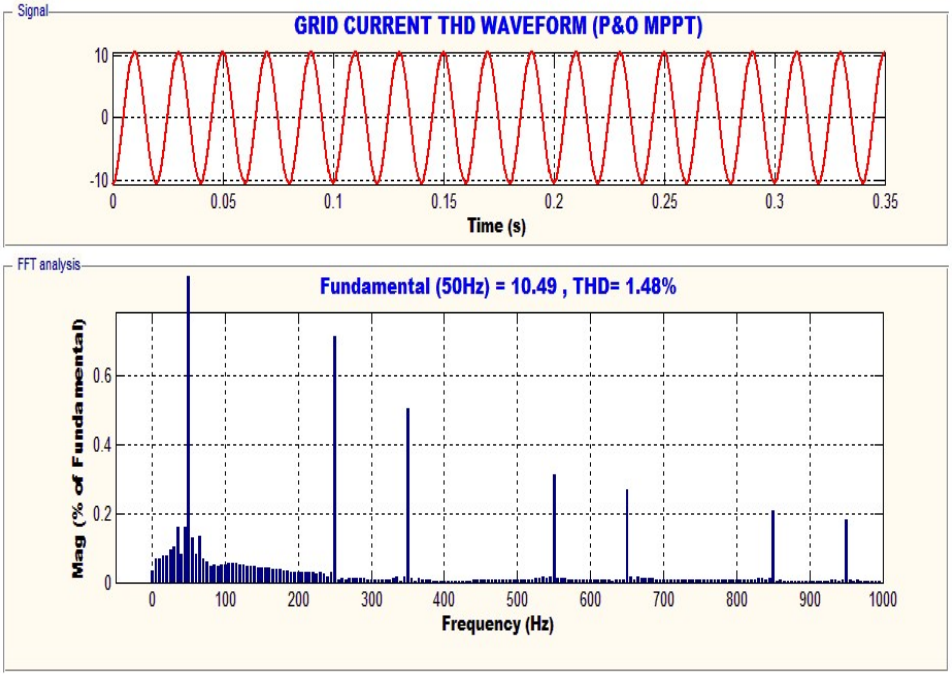

Fig 17. The P&O control technique to generate a grid current THD Waveform.

The provided diagram illustrates the grid current's Total Harmonic Distortion (THD) waveform, which is analyzed through FFT analysis. To Enhance the quality of electrical powerand meetIEEE harmonics standard, the expected method involves using a PI-based grid for stable voltage operation, a fuzzy logic-based Zeta converter for maximum power extraction and stable grid voltage, and a three-phase inverter. This approach significantly reduces the THD of the grid current, ensuring a stable and efficient PV system operation.

V. CONCLUSIONS

This article describes a micro-grid system that employs Renewable Energy Generation System (REGS) to supply electricity to remote and low-population areas. The system utilizes wind and solar energy units to generate power and deliver high-quality power to consumers automatically. This study provides information about the system's main component sizes. The system's performance is assessed under different load profiles and input conditions, and it has been demonstrated that the power quality is satisfactory at the load terminals. Additionally, the study presents laboratory prototype test results that demonstrate the system's effectiveness. Furthermore, the system's rotor-side converter and sensors are used to charge external batteries while achieving unity power factor rectifier operation.

REFERENCES

[1] S. Kumar Tiwari, B. Singh and P. K. Goel, "Design and Control of Microgrid Fed by Renewable Energy Generating Sources," in IEEE Transactions on Industry Applications, vol. 54, no. 3, pp. 2041-2050, May-June 2018, doi: 10.1109/TIA.2018.2793213.

[2] SAMIR KOURO, JOSE I. LEON and DMITRI VINNIKOV, Year: 2015, “Grid-Connected Photovoltaic Systems”, IEEE Transactions on industrial electronics, vol. 03, no. 4, pp. 47- 61.

[3] Ujjwal Kumar Kalla, Bhim Singh, S. Sreenivasa Murthy, Chinmay Jain and Krishan Kant, Year: 2018, “Adaptive Sliding Mode Control of Standalone Single-Phase Microgrid Using Hydro, Wind, and Solar PV Array-Based Generation”, IEEE Transactions on Smart Grid, vol. 9, no. 6, pp. 6806 – 6814.

[4] Benjamin Kroposki, Brian Johnson, Yingchen Zhang, VahanGevorgian, Paul Denholm, Bri-Mathias Hodge and Bryan Hannegan, Year: 2017, “Achieving a 100% Renewable Grid: Operating Elect. Power Systems with Extremely High Levels of Variable Renewable Energy”, IEEE Power and Energy Magazine, vol. 15, no. 2, pp. 61 – 73.

[5] Abdallah Tani, Mamadou BaïloCamara, Year: 2014, “Energy management in the Decentralized Generation Systems based on Renewable Energy -Ultracapacitors and Battery to compensate the wind/load power fluctuations”, IEEE Transactions on Industry Applications, pp. 01-11.

[6] Simon Camal, Andrea Michiorri and George Kariniotakis, Year: 2018, “Optimal Offer of Automatic Frequency Restoration Reserve from a Combined PV/Wind Virtual Power Plant”, IEEE Transactions on Power Systems, vol. 33, no. 6, pp. 6155 – 6170.

[7] Mukesh Gujar, Alekhya Datta and Parimita Mohanty, Year: 2013, “Smart Mini Grid: An innovative distributed generation-based energy system”, IEEE Innovative Smart Grid Technologies, pp. 1 – 5.

[8] José Antonio Aguado, Antonio Jose Sanchez Racero and Sebastián de la Torre, Year: 2018, “Optimal Operation of Electric Railways with Renewable Energy and Electric Storage Systems”, IEEE Transactions on Smart Grid, vol. 9, no. 2, pp. 993 – 1001.

[9] JussiEkström; Matti Koivisto; IlkkaMellin; Robert John Millar; Matti Lehtonen, Year: 2017, “A Statistical Model for Hourly Large-Scale Wind and Photovoltaic Generation in New Locations”, IEEE Transactions on Sustainable Energy, vol. 8, no. 4, pp. 1383 – 1393.

[10] S. Lenin Prakash, M. Arutchelvi and A. Stanley Jesudaiyan, Year: 2016, “Autonomous PV-Array Excited Wind-Driven Induction Generator for Off-Grid Application in India”, IEEE

Journal of Emerging and Selected Topics in Power Electronics, vol. 4, no. 4, pp. 1259 – 1269.
[11] Ashu Verma, Ram Krishan and Sukumar Mishra, Year: 2018, "A Novel PV Inverter Control for Maximization of Wind Power Penetration", IEEE Transactions on Industry Applications, vol. 54, no. 6, pp. 6364 – 6373.
[12] Yi Wang and Lie Xu, Year: 2012, "Coordinated Control of DFIG and FSIG-Based Wind Farms Under Unbalanced Grid Conditions", IEEE Transactions on Power Delivery, vol. 25, no. 1, pp. 367 – 377.
[13] Doaa M. Yehia, Diaa-Eldin A. Mansour and Weijia Yuan, Year: 2018, "Fault Ride-Through Enhancement of PMSG Wind Turbines with DC Microgrids Using Resistive-Type SFCL, IEEE Transactions on Applied Superconductivity, vol. 28, no. 4, pp. 245-256.
[14] Zhongqiu Wang, Gengyin Li, Gang Li and Hao Yue, Year: 2012, "Studies of multi-type composite energy storage for the photovoltaic generation system in a micro-grid", IEEE Transactions on Applied Superconductivity, pp. 791 – 796.
[15] S.K. Tiwari, Bhim Singh and P.K. Goel, Year: 2016, "Design and control of micro-grid fed by renewable energy generating sources", IEEE Transactions on Industry Applications, pp. 1 – 6.
[16] Da Fang, Weiyu Xu, Ling Bu and Lei Song, Year: 2016, "Input-parallel output-parallel DC-DC converter with MPPT technique for grid connection of multiple distributed generators", IEEE Transactions on Smart Grid, vol. 09, no. 3, pp. 2329 – 2333.
[17] Shankar R, Sengolrajan T, Mohanraj K, Balraj B,Integration of wind and solar farms in a DFIG using hybrid GA-ANN controllers,Electric Power Systems,Research, Volume 213, 2022, 108764, ISSN 0378-7796,https://doi.org/10.1016/j.epsr.2022.108764.